

# Solar Cell Efficiency Losses Due to Impurities From the Crucible in Multicrystalline Silicon

Florian Schindler, Bernhard Michl, Jonas Schön, Wolfram Kwapil, Wilhelm Warta, and Martin C. Schubert

**Abstract**—The electrical material quality of multicrystalline (mc) silicon for photovoltaic applications suffers from crystal defects as well as from impurities that originate from the feedstock, the quartz crucible, and its coating. In this study, we investigate the influence of impurities from the crucible on efficiency losses in mc silicon solar cells, focusing on the limitation due to iron. The applicability of *p*-type mc silicon, crystallized in G1 sized crucibles of industrial material quality and very pure electrically fused silica, for a high-efficiency solar cell process is examined by measuring lifetime and interstitial iron concentration in the wafers after different processing steps and by estimating the cell efficiency potential from injection-dependent bulk lifetime measurements. Interstitial iron concentrations extracted from 2-D simulations of iron precipitation at crystal defects and gettering during processing agree well with Fe<sub>i</sub> measurements at different process stages and explain the observations. Efficiency losses are quantified to losses due to segregated impurities diffused into the silicon melt, losses due to decorated crystal defects and losses due to solid-state diffusion into the crystal. By using a high-purity crucible, losses are reduced significantly and an efficiency gain of 0.5% absolute is estimated to be attainable on wafers with edge region.

**Index Terms**—Defects, gettering, high-efficiency solar cells, iron, lifetime, multicrystalline silicon.

## I. INTRODUCTION

IS multicrystalline silicon suited for the production of high-efficiency solar cells? Although feedstock quality and crystallization processes of mc silicon have improved significantly in recent years, its electrical material quality is still limited by metal impurities and crystal defects. As the feedstock purity is typically high enough (as shown in [1], the iron concentration in the crystallized silicon stemming from the feedstock is around one order of magnitude lower than the total iron concentration

in the crystal additionally accounting for diffusion of iron into the melt), the quartz crucible and the crucible coating remain the main sources for impurities. Several groups have been investigating the crucial role of crucible and coating on impurities in crystallized silicon [1]–[5]. Impurities can diffuse into the liquid silicon melt and during the crystallization be incorporated into the crystal lattice that lead to a background impurity concentration that increases toward the top of the crystal due to the very low segregation coefficients of metals. Additionally, solid-state diffusion from the crucible and its coating into the solidified part of the ingot takes place, leading to an edge region of very high impurity concentration and low bulk lifetimes. Both the background impurity concentration and the high concentration in the edge region limit the bulk lifetime, and thereby, material quality of multicrystalline silicon. As these impurities mainly stem from the crucible and its coating, improving the purity of both is one approach to reaching better electrical material quality, and thereby, higher cell efficiencies.

In this study, we investigate the influence of impurities from the crucible on solar cell efficiency losses in multicrystalline silicon. Therefore, the material quality of wafers from a block that was crystallized by directional solidification in a standard crucible is compared with the material quality of wafers from a block crystallized in a crucible of high purity. To separate the influence of the different crucible materials from other aspects that affect the material quality, the crystallizations were conducted under comparable conditions (temperature profiles, crystallization time, gas flows) in the same crystallization furnace, and a comparable crucible coating as well as the same silicon feedstock was used. While in this paper, the influence of the crucible system is discussed, the impact of the coating on contamination is separated from the influence of the crucible in [1], where we show that for the high-purity crucible, the finite impurity source provided by the coating is the main source of iron diffusing into the silicon melt, while for the standard crucible, the flux of iron from the crucible dominates after the consumption of iron from the coating. Impurity concentrations in the crucibles and the coating can also be found in [1] and [6]. The material quality is analyzed by imaging the bulk lifetime and the interstitial iron concentration during the solar cell process. The limitation due to interstitial iron is evaluated and bulk limited solar cell efficiency potentials are estimated by spatially resolved injection-dependent bulk lifetime measurements. Two different cell processes are compared, a standard PERC process with a phosphorous diffusion and a high-efficiency PERC approach where an additional oxidation for front-surface passivation is applied. Finally, the role of iron is discussed by elaborating the influence of iron on different cell parameters.

Manuscript received July 24, 2013; revised September 5, 2013; accepted September 24, 2013. This work was supported by the German Federal Ministry for the Environment, Nature Conservation and Nuclear Safety and by industry partners within the research cluster “SolarWinS” under Contract 0325270G.

F. Schindler and W. Kwapil are with the Fraunhofer Institut für Solare Energiesysteme, Freiburg 79110, Germany and also with Freiburger Materialforschungszentrum, Albert-Ludwigs-Universität Freiburg, Freiburg 79104, Germany (e-mail: florian.schindler@ise.fraunhofer.de; wolfram.kwapil@ise.fraunhofer.de).

B. Michl, J. Schön, W. Warta, and M. C. Schubert are with Fraunhofer Institut für Solare Energiesysteme, Freiburg 79110, Germany (e-mail: bernhard.michl@ise.fraunhofer.de; jonas.schoen@ise.fraunhofer.de; wilhelm.warta@ise.fraunhofer.de; martin.schubert@ise.fraunhofer.de).

Color versions of one or more of the figures in this paper are available online at <http://ieeexplore.ieee.org>.

Digital Object Identifier 10.1109/JPHOTOV.2013.2284060

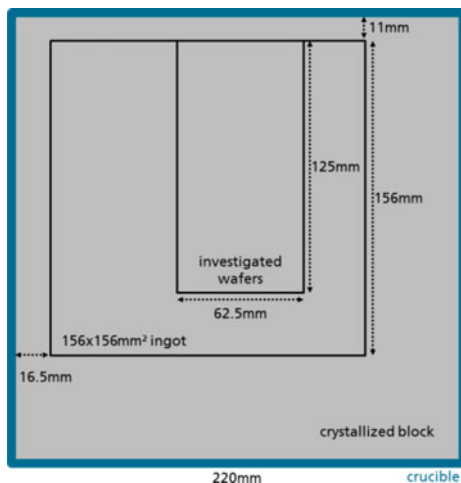


Fig. 1. Investigated wafers from G1 crystallization (top view).

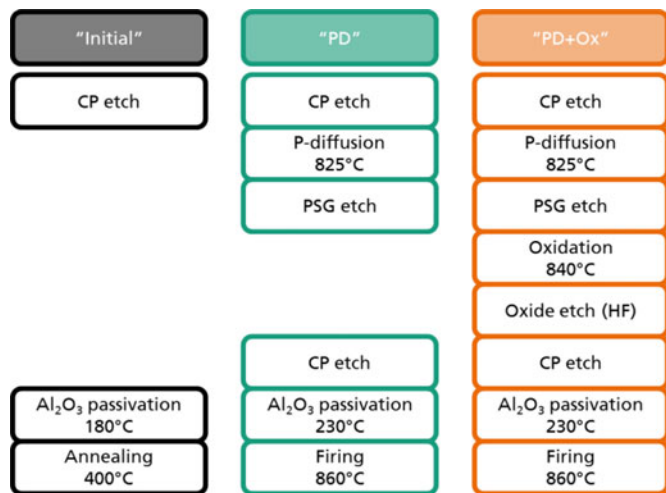


Fig. 2. Sample Processing. Diffusion, oxidation and etching are double-side processes.

## II. MATERIAL AND METHODS

For our investigations, boron-doped *p*-type multicrystalline material from two G1 crystallizations ( $\sim 220 \times 220 \times 128 \text{ mm}^3$ ) was used. The crystallizations differed only in the material quality of the crucibles, while the furnace and process recipe remained unchanged. One crystallization was realized in a crucible of standard industrial quality ("*SQ*"), the other one in a crucible of very high purity ("*HP*").

The ingots were cut asymmetrically from the block (cf., Fig. 1, view from above). In this paper, we focus on 125 mm  $\times$  62.5 mm-sized wafers, such that impurities diffused into the crystallized block by solid-state diffusion affect only one edge of the wafers (in the following referred to as "edge region"; the rest of the wafer, where no edge influence on bulk lifetime is visible, is denoted as "central region").

Fig. 2 shows the high-temperature processing steps of the different wafers. Three 125 mm  $\times$  62.5 mm sister wafers were chosen from each ingot as sketched in Fig. 1 and from a central block height. One served as ungettered reference ("*Initial*"), the

other two were subjected to all high-temperature steps including phosphorous diffusion of two different cell processes ("*PD*" and "*PD+Ox*") and served as lifetime samples for cell simulations. The only difference between "*PD*" and "*PD+Ox*" is the oxidation at 840 °C, which is applied to achieve better front-surface passivation in the solar cell. For the lifetime samples, the oxide films and emitter layers were etched away prior to passivating the samples with Al<sub>2</sub>O<sub>3</sub> in order to obtain lifetime samples with identically passivated surfaces. The passivation of the wafers from "*PD*" and "*PD+Ox*" was furthermore fired at a temperature of 860 °C. This ensures that all high-temperature steps of the corresponding solar cell process were applied to these wafers and the material quality corresponds to that of the final cells.

The high-temperature steps of "*PD*" correspond to those of a standard PERC process, while the additional oxidation in "*PD+Ox*" is a part of a high-efficiency PERC process with a lower front-surface recombination based on the additional oxide-passivation.

The material quality of each wafer was investigated by means of QSSPL-calibrated [7] photoluminescence imaging (PLI) [8] as described in [9] to obtain images of the minority charge carrier bulk lifetime and images of the interstitial iron concentration [10]. This also allows for imaging the relative carrier bulk lifetime limitation due to interstitial iron. For comparison, local concentrations of iron–boron pairs in as-grown wafers were measured with a conventional deep level transient spectroscopy (DLTS) [11] setup using the lock-in detection at Dresden University of Technology, Dresden, Germany. As DLTS-measurements are conducted in the dark, iron point defects should exist as FeB pairs, and therefore, measured FeB concentrations should be quantitatively comparable with Fe<sub>i</sub> concentrations obtained from lifetime measurements. Injection-dependent QSSPL-calibrated PLI allows for an estimation of the bulk limited cell efficiency potential by the "efficiency limiting bulk recombination analysis" (ELBA) [12] (with modifications described in [13]). Based on the injection-dependent bulk lifetime images, pseudoefficiencies are calculated via PC1D models. The cell structure is a passivated emitter and rear LFC cell with a honeycomb texture. The front, emitter, and back side recombination parameters and optics for the PC1D model "*PD+Ox*" are taken from [14]. In [14], the model was adjusted to measurements of external and internal quantum efficiency and reflection of a honeycomb textured LFC cell that featured also the "*PD+Ox*" front side. The emitter saturation current density  $J_{0e}$  calculated from  $J_{sc}$  and  $V_{oc}$  is 180 fA/cm<sup>2</sup> for the "*PD+Ox*" model. The "*PD*" model differs only from the "*PD+Ox*" model in the front and emitter recombination. These were adjusted to a  $J_{0e}$  of 630 fA/cm<sup>2</sup> measured on honeycomb textured samples with SiN<sub>x</sub> passivated emitter without oxidation. The higher value reflects the missing oxide passivation and the missing improvements of the emitter profile during the oxidation, which is especially important for a honeycomb texture due to the large surface area. The base doping of the cell models is taken from the mc samples,  $1.4 \times 10^{16} \text{ cm}^{-3}$  for the *SQ*-material and  $1.7 \times 10^{16} \text{ cm}^{-3}$  for the *HP*-material. This allows for a calculation of the pseudoefficiency limit of the cells (limit due to the cell

concept neglecting series resistance losses and bulk recombination, in the following described as “cell limit”). The pseudo-efficiency limit of “PD” is 20.0% for both materials; the limit of “PD+Ox” is slightly higher for the *HP* wafers (21.3%) than for the *SQ* wafers (21.2%). This is due to the higher doping of the *HP* wafers, and thus, higher  $V_{oc}$  values and will be taken into account when discussing the material related losses in Section III-B.

The 2-D simulations of the iron precipitation at crystal defects during the crystallization process and redistribution during further processing are performed with Sentaurus Process [15]. The comparison of simulation and measurement allows detailed analyses, and thus, a better understanding of the gettering processes. The Fe distributions before solar cell processing are taken from our experimentally verified simulations of the Fe contamination during the crystallization process [1]. For these simulations, only the measured iron concentrations in the crucible, coating, and feedstock are needed as input. In our model, for heterogeneous precipitation, iron silicide could nucleate at crystal structures that are inhomogeneously distributed in the 2-D model structure. We assume a mean grain width of 2 mm and a dislocation density of  $8 \times 10^3 \text{ cm}^{-2}$  as in previous simulations [16]. The Fokker–Planck equation, which is used for iron precipitates of different size [17], enables us to predict the precipitate size distributions, the growth rates, and thus, the decrease of the interstitial iron concentration [18]. For the simulation of the phosphorus diffusion, the predictive model from [19] is used. The phosphorus diffusion gettering model, based on segregation, is taken from [20].

All model parameters, like the segregation coefficient of iron for PDG [20] and the parameters that describe the precipitation at crystal defects [16], [17], [21] are taken from former model calibrations. Thus, the simulations are performed independently of the measurements, using the known temperature profiles as input parameters. For the comparison with the measurements, we averaged the simulated interstitial iron concentration in the 2-D structure excluding the emitter.

### III. RESULTS

#### A. Defect Redistribution During the Solar Cell Process

In order to understand the role of impurities for efficiency losses in mc silicon solar cells, in a first step, the impact of high-temperature steps on the impurity distribution in the wafers has to be analyzed. This is done in detail in this section.

Images of bulk lifetime, concentration of interstitial iron, and fraction of recombination due to interstitial iron compared with the total recombination  $\frac{\tau_{eff}}{(\tau_{SRH, Fe_i})}$  are evaluated in the as-grown state, after a phosphorous diffusion and after a phosphorous diffusion followed by an additional oxidation (cf., Fig. 3). Images of carrier bulk lifetime and fraction of recombination due to  $Fe_i$  are taken at a constant generation rate of 0.1 suns, which is estimated to correspond to an injection level close to (maximum power point) MPP-conditions in the solar cell.

1) *Before High-Temperature Processing (“Initial”)*: A significant difference in the material quality of *SQ*- and *HP* wafers is visible prior to any gettering or high-temperature step (“ini-

tial”). The *HP* wafers feature significantly higher bulk lifetimes, lower concentrations of interstitial iron, and a much smaller edge region (see first row in Fig. 3).

2) *After Gettering (“PD”)*: During the phosphorous diffusion, impurities are gettered efficiently in both materials, which leads to higher bulk lifetimes and lower  $Fe_i$  concentrations across the whole wafers as well as to a significant reduction of the width of the edge region (see second row of Fig. 3). Because of the efficient gettering, the difference in material quality of *SQ* and *HP* wafers is smaller than in the as-cut state, but the influence of the edge region is still significant for the *SQ*-material.

3) *After Gettering and Oxidation (“PD+Ox”)*: Applying an oxidation at 840 °C leads to “poisoning” [22], [23] of the bulk material in both the *HP* as well as the *SQ* wafers (see third row of Fig. 3). This high-temperature step can dissolve iron-precipitates and iron-agglomerations at crystal defects, formed during the crystallization, and leads to a back-diffusion of previously gettered iron from the phosphorous layer into the silicon bulk that leads to a higher concentration of interstitial iron across the whole wafers. In addition, the edge zone becomes wider in both materials compared with “PD.” Still, after the oxidation the *HP* wafers feature better material quality than the *SQ* wafers, both in good grains as well as in the edge region of the wafers, and the edge region is much smaller.

4) *Comparison with Simulations*: We compare the experimentally observed effects with simulations with Sentaurus Process [15] as described in Section II. Fig. 4 shows the measured concentrations of interstitial iron in both materials, averaged in the central region (circles) and in the edge of the wafers (triangular symbols), as well as the corresponding simulated concentrations before and after the different high-temperature steps (open symbols). The simulations are in very good agreement with our measurements for values of interstitial iron concentrations above  $10^{11} \text{ cm}^{-3}$  for the *SQ*-material, deviations occur for the *HP*-material and for low concentrations of interstitial iron below  $10^{10} \text{ cm}^{-3}$ . This is due to different reasons: experimental values below  $10^{10} \text{ cm}^{-3}$ , as measured in the central region of the *HP* wafers after diffusion, are in the range of the detection limit and should be interpreted as upper limit for  $Fe_i$  concentrations. As the visible edge region in the *HP* wafers is very small and does not reach the plateau of constant interstitial iron concentration as in the case of the *SQ* wafers, here experimental values were extracted from the very edge of the wafer. However, the distance from the crucible wall is not known exactly. A deviation in the distance from the crucible between measurements and simulations might explain the differing values in the edge region, as a small deviation in the distance leads to a significant deviation in the concentration of interstitial iron. Still, both measurements and simulations show the same trend, an increasing concentration of interstitial iron in the edge region after the oxidation. As a further verification for the interstitial iron concentrations determined from carrier lifetime measurements, we include in Fig. 4 values for [FeB] that are determined from DLTS in as-grown *SQ* wafers. Excellent agreement is found for measurements in the edge region. In the central region, the high detection limit of DLTS ( $4 \times$

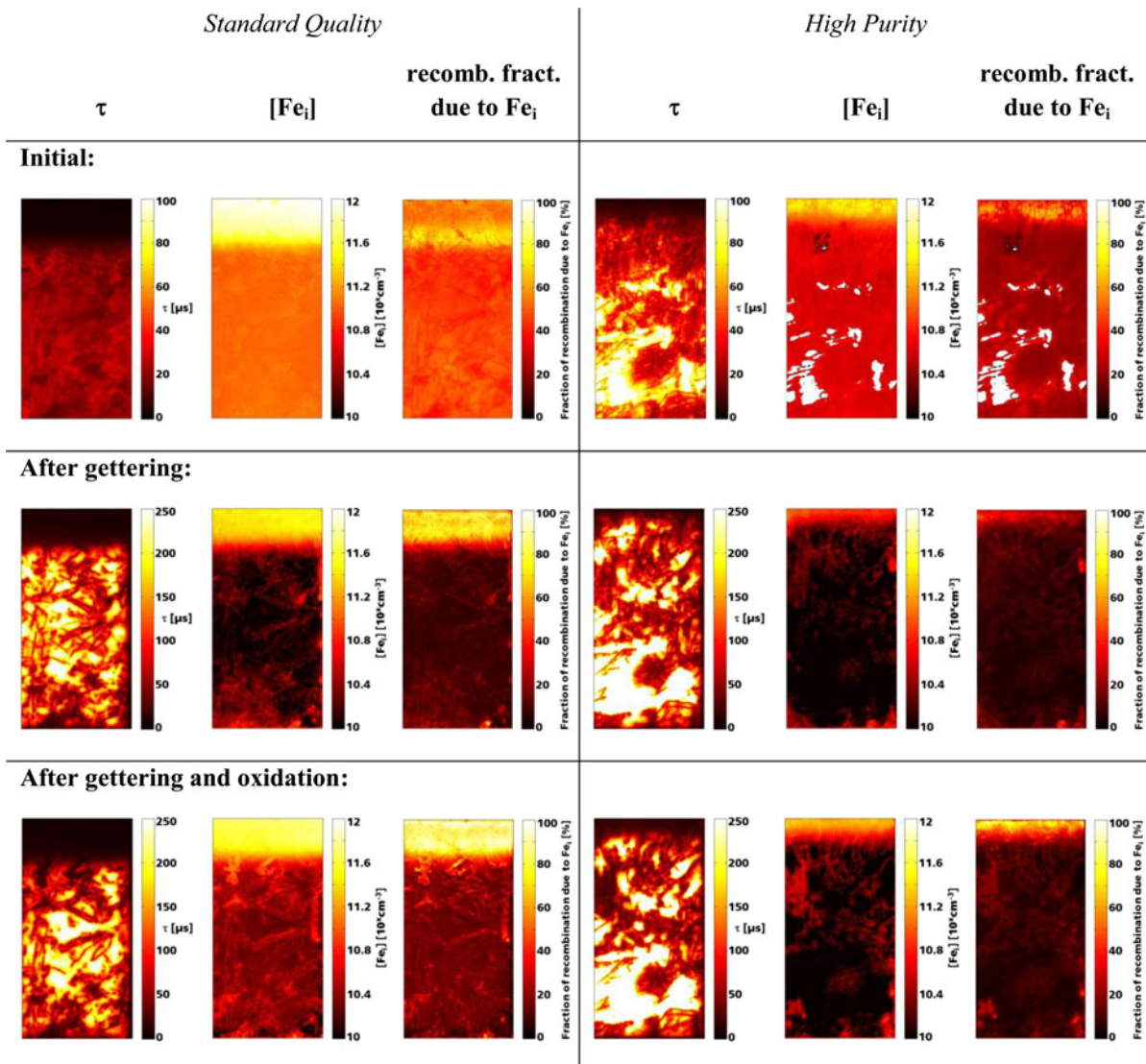


Fig. 3. Images of the bulk lifetime at 0.1 suns generation, the interstitial iron concentration and the fraction of recombination due to interstitial iron compared with the total recombination at 0.1 suns generation in the two materials after different processing steps. (upper row) Initial. (middle row) After phosphorous diffusion. (lower row) After phosphorous diffusion and oxidation. (left half) *SQ* wafers. (right half) *HP* wafers.

$10^{11} \text{ cm}^{-3}$  for this sample) does not allow a quantitative comparison with iron imaging. The value determined by iron imaging is significantly lower than the DLTS detection limit ( $1.1 \times 10^{11} \text{ cm}^{-3}$ ).

5) *Role of Interstitial Iron*: The role of interstitial iron as recombination channel can be evaluated by measuring the fraction of recombination due to interstitial iron compared with the total carrier recombination in the wafers  $\frac{\tau_{\text{eff}}}{(\tau_{\text{SRH, Fe}_i})}$ . This is shown in the third and sixth column in Fig. 3. After gettering and oxidation, in the edge region, about 60%–70% of the total recombination is due to  $\text{Fe}_i$  in the *HP*-material and even 80%–90% in the *SQ*-material. In the central region, recombination via  $\text{Fe}_i$  is less important (15%–20% for *SQ* and less than 10% for *HP*). These results highlight the prominent role of iron as a recombination channel in multicrystalline silicon wafers, especially in crystal regions close to the crucible. As in the central region of the *HP* wafers, limitations are mainly due to crystal

defects decorated with metal impurities, the impurity transport from the crystallization environment into the silicon bulk has to be reduced even further. This indicates that besides a high-purity crucible also a crucible coating of highest purity has to be used [1].

### B. Bulk Limited Cell Efficiency Potential

As discussed in the previous section, the additional oxidation harms the material quality of mc wafers. On the other hand, the oxidation leads to a significantly better front-surface passivation in the solar cell. Hence, for a prediction of cell performances, material limitations as well as limitations due to the cell concept have to be taken into account. This is done by an “ELBA” [12], [13], which combines measurements of spatially resolved and injection-dependent bulk lifetime with a cell-simulation based on PC1D as explained in Section II.

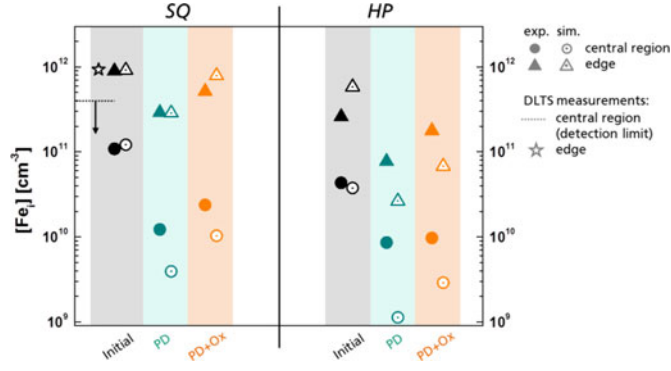


Fig. 4. Averaged concentrations of interstitial iron in the two materials after different processing steps. The left half of the graph shows the results of the wafers from the standard quality crucible, the right half the results of the wafers from the high-purity crucible. Experimental results determined from carrier lifetime measurements are shown with closed symbols, simulations with Sentaurus Process of the interstitial iron concentrations are shown with open symbols. Measured values below  $1 \times 10^{10} \text{ cm}^{-3}$  are in the range of the detection limit and should be interpreted as upper limit for  $\text{Fe}_i$  concentrations. Excellent agreement is found for values determined from DLTS on as grown *SQ* wafers.

TABLE I  
GLOBALLY AVERAGED CELL PARAMETERS SIMULATED FROM  
INJECTION-DEPENDENT BULK LIFETIME MEASUREMENTS

	<i>SQ</i> PD	<i>SQ</i> PD+Ox	<i>HP</i> PD	<i>HP</i> PD+Ox
$V_{oc}$ [mV]	625	639	628	646
$J_{sc}$ [mA/cm <sup>2</sup> ]	36.7	37.0	37.1	37.5
$\text{PPF}_{\text{bulk}}$ [%]	82.7	82.4	83.0	82.8
$\text{P}\eta_{\text{bulk}}$ [%]	<b>19.0</b>	<b>19.5</b>	<b>19.3</b>	<b>20.1</b>
cell limit [%]	20.0	21.2	20.0	21.3
$\eta$ loss [% abs.]	-1.0	-1.7	-0.7	-1.2

Modeling the open-circuit voltage  $V_{oc}$ , the short-circuit current  $J_{sc}$ , the pseudofill factor  $\text{PPF}_{\text{bulk}}$  (neglecting series resistance losses, only lower than ideal fill factor due to injection-dependent bulk recombination), and the pseudoefficiency  $\text{P}\eta_{\text{bulk}}$  (neglecting series resistance losses) from the injection-dependent bulk lifetimes and averaging across the wafer delivers the results listed in Table I for the mc wafers.

These values can be discussed more clearly by taking a look at the spatially resolved simulated pseudoefficiency  $\text{P}\eta_{\text{bulk}}$ . Fig. 5(a) shows  $\text{P}\eta_{\text{bulk}}$  for the *SQ* wafer, while Fig. 5(b) for the *HP* wafer. The left half of the images refers to the cell process without oxidation, the right half to the high-efficiency cell process. Both materials benefit from the additional front-surface passivation, which leads to a strong increase in  $V_{oc}$  (cf., first row in Table I) that is visible in a homogeneous increase in efficiencies in the good grains. On the other hand, as the material quality suffers from the high-temperature oxidation, the efficiency potential decreases at dislocation clusters and in the edge region. This is also reflected in a slight decrease in the  $\text{PPF}_{\text{bulk}}$  after the oxidation in both materials and a rather small gain in  $J_{sc}$ . As we will discuss in more detail in Section III-C,  $\text{PPF}_{\text{bulk}}$  and  $J_{sc}$  are especially influenced by low lifetime regions due to a strong injection dependence of recombination

at defects like interstitial iron. This also explains why  $\text{PPF}_{\text{bulk}}$  and  $J_{sc}$  suffer more strongly from the degraded material quality after the oxidation than  $V_{oc}$ .

Now, we are able to discuss the origin of the efficiency losses after the high-temperature oxidation in detail. Therefore, we evaluated the efficiency potential in the best  $1 \text{ cm} \times 1 \text{ cm}$  area, which is virtually void of crystal defects in both materials. The loss compared with the cell limit can be attributed to segregated impurities remaining after processing that diffused into the liquid silicon melt before crystallization [see first (orange) part of the columns in Fig. 6]. To assess the influence of crystal defects such as dislocations and grain boundaries, in a second step, the efficiency potential in the central region (without any edge influence) is evaluated. The additional loss can then be attributed to recombination via impurities at dislocations and grain boundaries [see second (cyan) part of the columns in Fig. 6]. In a last step, by evaluating the efficiency potential of the whole wafer, also the edge region, and therefore, the efficiency loss due to impurities diffused into the crystal by solid-state diffusion is taken into account [see third (gray) part of the columns in Fig. 6].

The main losses in the *SQ*-material are the remaining segregated impurities that had diffused into the melt before crystallization ( $-0.6\%$  abs.) and impurities diffused into the solidified crystal by solid-state diffusion visible in the large edge region (width on the wafer  $\sim 25 \text{ mm}$ ;  $-0.6\%$  abs.). In contrast, in the *HP*-material, the main losses can be attributed to recombination active crystal defects like dislocation clusters and grain boundaries ( $-0.7\%$  abs.). In total, the losses sum up to  $-1.7\%$  abs. in the *SQ*-material and  $-1.2\%$  abs. in the *HP*-material, which lead to a significantly higher efficiency potential in the *HP*-material of  $20.1\%$  compared with  $19.5\%$  in the *SQ*-material (additional  $+0.1\%$  abs. due to higher doping in *HP*). As the losses in the *HP*-material related to decorated crystal defects are even higher than in the *SQ*-material (*HP*:  $-0.7\%$  abs.; *SQ*:  $-0.5\%$  abs.), the benefit from purer crucible materials could be even stronger if the crystal quality of both materials was comparable. In this specific case, the same temperature profiles for crystallization were used for *SQ* and *HP* without optimizing the profile for the thinner *HP* crucible. This might be a reason for the worse crystal quality of the *HP*-material. In general, using a high-purity crucible should not impact the crystal quality if the temperature profiles were adapted to the thinner crucible.

As we measured concentrations of interstitial iron, we can now evaluate its impact also on the cell level. To do so, we performed the same simulations as previously mentioned with the measured concentration of interstitial iron as the only bulk lifetime limiting recombination channel (input for cell simulation: injection-dependent images of  $\tau_{\text{SRH,Fe}_i}$ ). The result can be seen in Fig. 6 as the shaded fractions of the columns, which express the corresponding efficiency losses due to interstitial iron. A major part of the losses due to segregated impurities that had diffused into the melt can be attributed to interstitial iron ( $\sim 40\%$  for both materials), losses due to the edge region are even dominated by interstitial iron ( $\sim 90\%$ ). In contrast, interstitial iron plays a minor role for losses due to decorated defects. However, these losses might also be attributed to iron or iron precipitates bound to crystal defects.

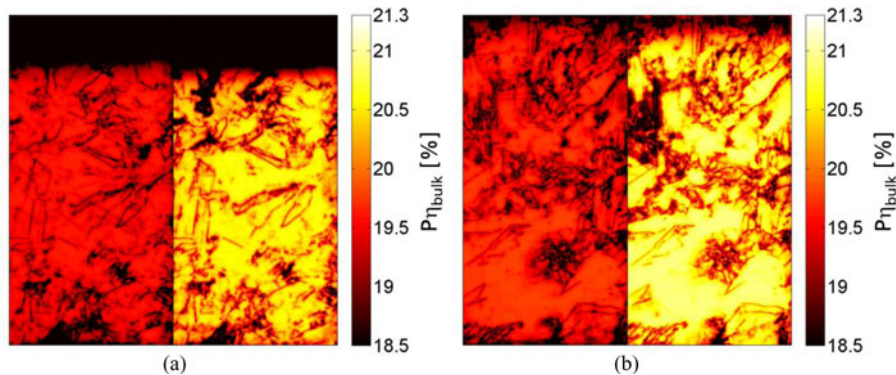


Fig. 5. Spatially resolved simulated cell efficiency potential ( $P\eta_{\text{bulk}}$ ). The left half of the images refers to the cell process without oxidation (“PD”), the right half with the additional oxidation (“PD+Ox”). (a) Standard quality crucible (b) High-purity crucible.

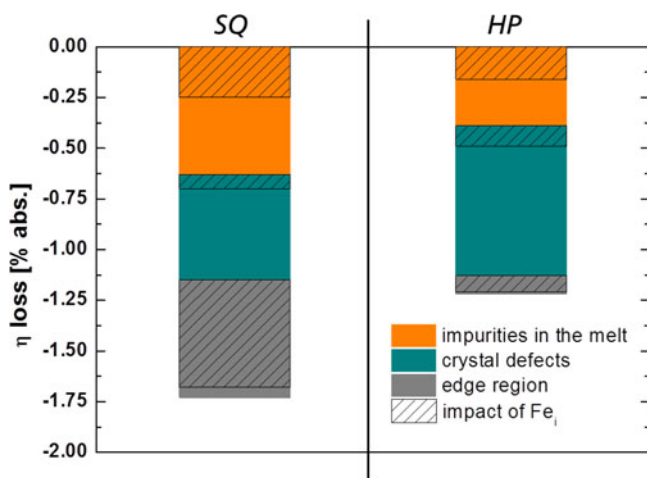


Fig. 6. Efficiency losses in multicrystalline silicon from (left) standard crucible and from (right) high-purity crucible.

### C. Injection-Dependent Impact of Interstitial Iron on Cell Parameters

As already shown in the previous section, interstitial iron plays a major role concerning efficiency losses in mc silicon. In the following, we want to shed more light on the injection dependence of recombination via  $\text{Fe}_i$  and its meaning for the different solar cell parameters. Therefore, we analyzed injection-dependent bulk lifetimes on two different spots of the *HP* wafer after phosphorous diffusion and oxidation (cf., Fig. 7). Trends for the *SQ* wafer are the same and will, therefore, not be discussed here. Spot 1 with some good grains as well as some dislocations and grain boundaries features a medium bulk lifetime at 0.1 suns and a low to medium concentration of interstitial iron, whereas spot 2 features a high concentration of interstitial iron due to its closer position to the crucible wall. In Fig. 7, injection-dependent bulk lifetimes in the two spots (square root harmonic mean) are shown and compared with the SRH limit (including Auger recombination) due to the measured concentration of interstitial iron on the same spots. The spatially resolved  $\text{Fe}_i$  concentrations were recalculated according to the SRH theory with the parameters published by Istratov

*et al.* [24] including Auger recombination to spatially resolved and injection-dependent bulk lifetimes, which were then averaged according to a square root harmonic mean. This ensures that calculated bulk lifetimes from  $\text{Fe}_i$  are averaged like the measured bulk lifetimes.

Because of the higher concentration of interstitial iron, spot 2 features a much stronger injection dependence than spot 1. The injection dependence of the  $\text{Fe}_i$ -limited bulk lifetime shows a very similar trend compared with the measured bulk lifetime supporting the accuracy of measurements of the interstitial iron concentration by means of FeB pairing, as this curve does not depend on the splitting and pairing of FeB pairs. A very important point has to be emphasized here: measured bulk lifetimes on spot 2 are higher than on spot 1 for generation rates above one sun (injection levels higher than  $10^{15} \text{ cm}^{-3}$  in the graph), while this is not the case for lower injection due to the stronger impact of interstitial iron. This is of utmost importance for material characterization, as the injection level under MPP conditions in a solar cell made from this wafer is around  $3 \times 10^{13} \text{ cm}^{-3}$ . This means that bulk lifetimes measured at an injection level above  $10^{15} \text{ cm}^{-3}$  would lead to misleading interpretations of the material quality. Bulk lifetimes in the low injection regimes that represent MPP or  $J_{\text{sc}}$  conditions are easily accessible experimentally by using the self-consistent QSSPL-calibration, while a quasi-steady-state photoconductance measurement [25] could be affected by trapping at these injection levels.

Fig. 7(d) shows the fraction of recombination due to interstitial iron ( $\text{FoR}_{\text{Fe}_i}$ , SRH- and Auger-recombination considered) as a function of excess carrier density. While the dependence of injection level is rather low for spot 1, the limitation due to interstitial iron is increasing strongly for lower injection levels on spot 2. This behavior is crucial for the solar cell parameters, as has also been discussed by Macdonald *et al.* in [26]. While the influence of interstitial iron on  $V_{\text{oc}}$  is rather small (high injection level above  $10^{14} \text{ cm}^{-3}$ ,  $\text{FoR}_{\text{Fe}_i}$  around 30%), it affects  $J_{\text{sc}}$ , MPP, and the fill factor more strongly (cf., Table I) as the excess carrier density is much lower under these conditions ( $\text{FoR}_{\text{Fe}_i}$  around 60%). For even lower injection levels,  $\text{Fe}_i$  becomes the most dominant recombination channel ( $\text{FoR}_{\text{Fe}_i}$  around 80% for an excess carrier density of  $10^{12} \text{ cm}^{-3}$ ).

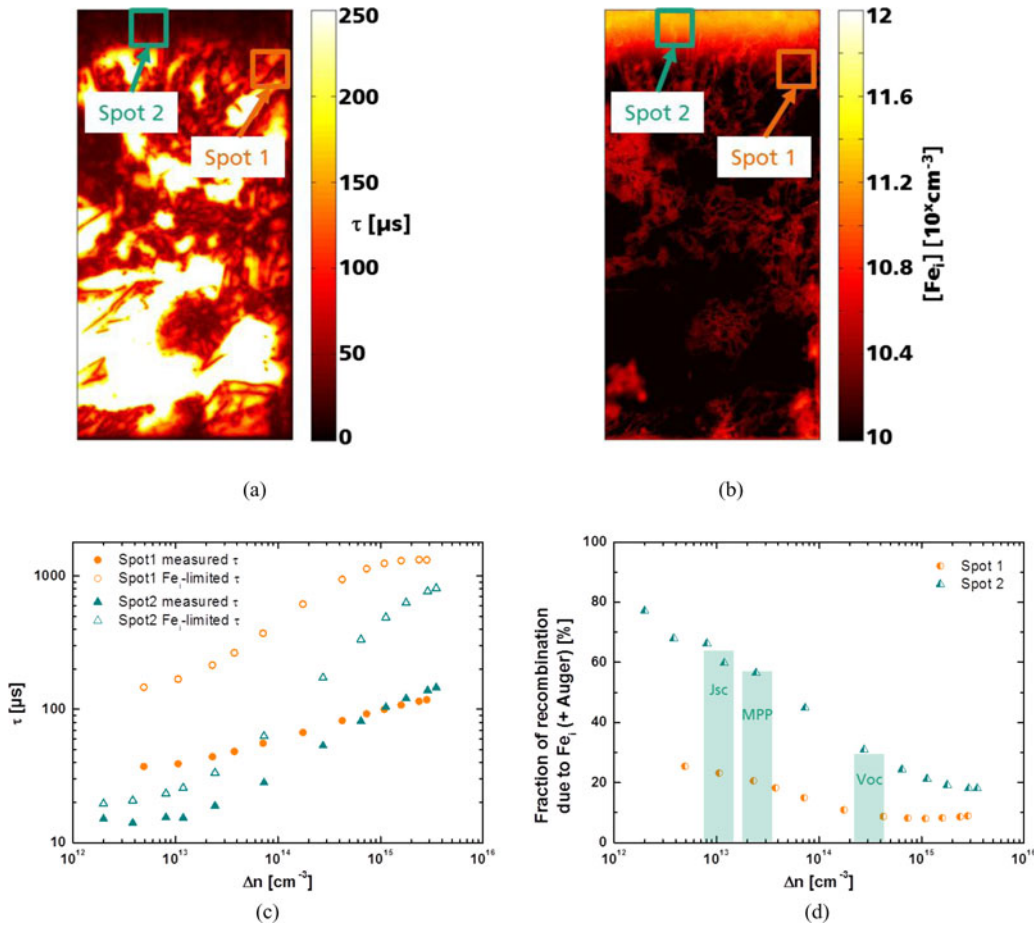


Fig. 7. Injection-dependent bulk lifetimes on different spots of a wafer compared with the SRH limit due to the concentration of interstitial iron [24] on the same spot. Spot 1 features a rather flat dependence on the injection level and a low limitation due to interstitial iron, while Spot 2 shows a strong injection dependence of bulk lifetime due to the higher concentration of interstitial iron. The fraction of recombination due to interstitial iron increases strongly for lower injection levels. (a) Bulk lifetime map at 0.1 suns. (b)  $\text{Fe}_i$  map. (c) Injection-dependent bulk lifetime. (d) Limitation due to  $\text{Fe}_i$ .

It has to be kept in mind that these evaluations only treat the concentration of interstitial iron. The total impact of iron will be even stronger, especially for higher injection levels, as here the role of iron precipitates becomes more important compared with interstitial iron [27]. This highlights the dominant role of iron as a recombination active impurity in multicrystalline silicon.

#### IV. CONCLUSION

In this study, we showed for G1 sized crucibles that efficiency losses in multicrystalline silicon can be reduced by crystallizing the silicon in crucibles of pure material quality (electrically fused silica). The loss in good grains due to remaining segregated impurities that had diffused into the silicon melt is reduced by around 40%. Additionally, the wider edge region in material from standard quality crucibles plays a crucial role, in our case losses due to the edge region are reduced by 85% in the material from the high-purity crucible, mainly because the size of the edge region on the wafers decreases from about 25 to 6 mm. However, as the crystal structure of the material from the standard crucible is better, losses due to decorated crystal defects are larger in the material from the high-purity crucible. This

should be avoidable by applying a better crystallization process. Limitations like crystal defects decorated with metal impurities indicate that besides a high-purity crucible also a crucible coating of highest purity has to be used to reduce the impurity transport from the crystallization environment into the silicon bulk as far as possible.

In the industry, larger crucibles, e.g., G6, are used. On the basis of the experimentally validated simulations, our results on G1 blocks can be transferred directly to these ingot sizes. Our general conclusions remain valid as the major part of the wafers will still be influenced by the edge region (20 from 36 wafers in G6 are “edge wafers”) and the edge region itself even becomes wider. However, the width of the edge region in the wafers depends strongly on the fraction cut off from the entire block. Further details on the transfer to larger crucible sizes can be found in [1]. The cost difference between the standard quality and the high-purity crucible is difficult to assess, as the high-purity crucible used for this study was a custom product for laboratory experiments.

Additionally, we elaborated on the role of interstitial iron and showed that it plays a major role for losses due to segregated impurities and dominates the losses in the edge region. At crystal

defects, impurities other than interstitial iron are dominating the losses, which likely are iron precipitates or iron bound to dislocations or grain boundaries.

The strong injection dependence of recombination at interstitial iron is crucial for the solar cell parameters: while  $V_{oc}$  is weakly influenced,  $Fe_i$  affects  $J_{sc}$ , MPP, and the fill factor more strongly.

#### ACKNOWLEDGMENT

The authors would like to thank T. Mchedlidze from Dresden University of Technology for the DLTS-measurements.

#### REFERENCES

- [1] M.C. Schubert, J. Schön, F. Schindler, W. Kwapil, A. Abdollahinia, B. Michl, S. Riepe, C. Schmid, M. Schumann, S. Meyer, and W. Warta, "Impact of impurities from crucible and coating on mc-silicon quality—The example of iron and cobalt," *J. Photovolt.*, vol. 3, no. 4, pp. 1250–1258, Oct. 2013.
- [2] B. Geyer, G. Schwichtenberg, and A. Muller, "Increased wafer yield in silicon ingots by the application of high purity silicon nitride-coating and high purity crucibles," in *Proc. IEEE 31st Photovolt. Spec. Conf.*, Orlando, FL, USA, 2005, pp. 1059–1061.
- [3] E. Olsen and E. J. Øvrelid, "Silicon nitride coating and crucible—Effects of using upgraded materials in the casting of multicrystalline silicon ingots," *Progr. Photovolt., Res. Appl.*, vol. 16, pp. 93–100, 2008.
- [4] T. Naerland, L. Arnberg, and A. Holt, "Origin of the low carrier lifetime edge zone in multicrystalline PV silicon," *Progr. Photovolt., Res. Appl.*, vol. 17, pp. 289–296, 2009.
- [5] R. Kvande, L. Arnberg, and C. Martin, "Influence of crucible and coating quality on the properties of multicrystalline silicon for solar cells," *J. Crystal Growth*, vol. 311, pp. 765–768, 2009.
- [6] M. Schumann, S. Meyer, C. Schmid, F. Haas, S. Riepe, and A. Cröll, "Impurity control of quartz crucible coatings for directional solidification of silicon," in *Proc. 27th Eur. Photovolt. Sol. Energy Conf. Exhib.*, Frankfurt, Germany, 2012, pp. 1049–1053.
- [7] T. Trupke, R. A. Bardos, and M. D. Abbott, "Self-consistent calibration of photoluminescence and photoconductance lifetime measurements," *Appl. Phys. Lett.*, vol. 87, pp. 184102-1–184102-3, 2005.
- [8] T. Trupke, R. A. Bardos, M. C. Schubert, and W. Warta, "Photoluminescence imaging of silicon wafers," *Appl. Phys. Lett.*, vol. 89, pp. 044107-1–044107-3, 2006.
- [9] J.A. Giesecke, M. C. Schubert, B. Michl, F. Schindler, and W. Warta, "Minority carrier lifetime imaging of silicon wafers calibrated by quasi-steady-state photoluminescence," *Sol. Energy Mater. Sol. Cells*, vol. 95, pp. 1011–1018, 2011.
- [10] D. Macdonald, J. Tan, and T. Trupke, "Imaging interstitial iron concentrations in boron-doped crystalline silicon using photoluminescence," *J. Appl. Phys.*, vol. 103, pp. 073710-1–073710-7, 2008.
- [11] D. V. Lang, "Deep-level transient spectroscopy: A new method to characterize traps in semiconductors," *J. Appl. Phys.*, vol. 45, pp. 3023–3032, 1974.
- [12] B. Michl, M. Rüdiger, J. Giesecke, M. Hermle, W. Warta, and M. C. Schubert, "Efficiency limiting bulk recombination in multicrystalline silicon solar cells," *Sol. Energy Mater. Sol. Cells*, vol. 98, pp. 441–447, 2012.
- [13] B. Michl, M. Kasemann, W. Warta, and M. C. Schubert, "Wafer thickness optimization for silicon solar cells of heterogeneous material quality," *Physica Status Solidi, Rapid Res. Lett.*, 2013, [Online]. DOI: 10.1002/pssr.201308090.
- [14] H. Hauser, B. Michl, S. Schwarzkopf, V. Kübler, C. Müller, M. Hermle, and B. Bläsi, "Honeycomb texturing of silicon via nanoimprint lithography for solar cell applications," *IEEE J. Photovolt.*, vol. 2, no. 2, pp. 114–122, Apr. 2012.
- [15] Synopsys, Sentaurus TCAD, release G-2012.06, Zurich, Switzerland, 2012.
- [16] J. Schön, H. Habenicht, M.C. Schubert, and W. Warta, "Understanding the distribution of iron in multicrystalline silicon after emitter formation: Theoretical model and experiments," *J. Appl. Phys.*, vol. 109, pp. 1–8, 2011.
- [17] A. Haarahiltunen, H. Väinölä, O. Anttila, M. Yli-Koski, and J. Sinkkonen, "Experimental and theoretical study of heterogeneous iron precipitation in silicon," *J. Appl. Phys.*, vol. 101, pp. 043507-1–043507-6, 2007.
- [18] J. Schön, A. Haarahiltunen, H. Savin, D. P. Fenning, T. Buonassisi, W. Warta, and M. C. Schubert, "Analyses of the evolution of iron-silicide precipitates in multicrystalline silicon during solar cell processing," *IEEE J. Photovolt.*, vol. 3, no. 1, pp. 131–137, Jan. 2013.
- [19] J. Schön, A. Abdollahinia, R. Müller, J. Benick, M. Hermle, W. Warta, and M. C. Schubert, "Predictive simulation of doping processes for silicon solar cells," *Energy Procedia*, vol. 38, pp. 312–320, 2013.
- [20] J. Schön, M. C. Schubert, W. Warta, H. Savin, and A. Haarahiltunen, "Analysis of simultaneous boron and phosphorus diffusion gettering in silicon," *Physica Status Solidi A*, vol. 207, pp. 2589–2592, 2010.
- [21] A. Haarahiltunen, H. Talvitie, H. Savin, O. Anttila, M. Yli-Koski, M. I. Asghar, and J. Sinkkonen, "Gettering of iron in silicon by boron implantation," *J. Mater. Sci. Mater. Electron.*, vol. 19, pp. S41–S45, 2008.
- [22] D. Macdonald, A. Cheung, and A. Cuevas, "Gettering and poisoning of silicon wafers by phosphorus diffused layers," in *Proc. 3rd World Conf. Photovolt. Energy Convers.*, 2003, vol. 2, pp. 1336–1339.
- [23] B. Michl, J. Schön, W. Warta, and M. C. Schubert, "The impact of different diffusion temperature profiles on iron concentrations and carrier lifetimes in multicrystalline silicon wafers," *IEEE J. Photovolt.*, vol. 3, no. 2, pp. 635–640, Apr. 2013.
- [24] A. A. Istratov, H. Hieslmair, and E. R. Weber, "Iron and its complexes in silicon," *Appl. Phys. A (Mater. Sci. Process.)*, vol. A69, pp. 13–44, 1999.
- [25] R. A. Sinton and A. Cuevas, "Contactless determination of current-voltage characteristics and minority-carrier lifetimes in semiconductors from quasi-steady-state photoconductance data," *Appl. Phys. Lett.*, vol. 69, pp. 2510–2512, 1996.
- [26] D. Macdonald and A. Cuevas, "Reduced fill factors in multicrystalline silicon solar cells due to injection-level dependent bulk recombination lifetimes," *Progr. Photovolt., Res. Appl.*, vol. 8, pp. 363–375, 2000.
- [27] W. Kwapil, J. Schön, F. Schindler, W. Warta, and M. C. Schubert, "Impact of Fe precipitates on injection-dependent carrier lifetime in mc-Si wafers analyzed by means of finite element simulations," *J. Photovolt.*, 2013, submitted for publication.

Authors' photographs and biographies not available at the time of publication.